Melting scenarios for three-dimensional dusty plasma clusters

André Schella, Tobias Miksch, and André Melzer
Institut für Physik, Ernst-Moritz-Arndt-Universität Greifswald, D-17489 Greifswald, Germany

Jan Schablinski, Dietmar Block, and Alexander Piel
Institut für Experimentelle und Angewandte Physik, Christian-Albrechts-Universität zu Kiel, D-24098 Kiel, Germany

Hauke Thomsen, Patrick Ludwig, and Michael Bonitz
Institut für Theoretische Physik und Astrophysik, Christian-Albrechts-Universität zu Kiel, D-24098 Kiel, Germany
(Received 30 June 2011; published 2 November 2011)

The melting transition of finite three-dimensional dust clouds (Yukawa balls) from a solid-like to a liquid-like state is systematically studied with high spatial and temporal resolution of the individual grains by means of stereoscopy. Two different melting scenarios are reported: Melting is induced first by an increase of plasma power, and second by laser-induced heating. The experiments confirm that melting starts with a loss of orientational correlation, followed by a loss of the radial order upon further heating. While the plasma-power melting is driven via the ion wakefield, laser heating provides a more equilibrium scenario. The internal loss of correlations is well captured by the triple correlation function (TCF) which is insensitive to particle exchanges and the rotation of the cluster as a whole. The critical Coulomb coupling parameter for $N = 35$ is determined as $\Gamma_{\mathrm{crit}} \approx 570$. The experimental findings are in good agreement with thermodynamic Monte Carlo simulations.

DOI: 10.1103/PhysRevE.84.056402 PACS number(s): 52.27.Lw, 64.60.an

I. INTRODUCTION

Dusty or complex plasmas allow for direct insight into correlated many-particle processes, which are relevant to many other fields including condensed matter physics, mesoscopic quantum systems, as well as the physics of colloidal suspensions (e.g., Refs. [1–3] and references therein). Typically, laboratory dusty plasmas are generated using melamine-formaldehyde (MF) particles of micron size immersed in a gaseous plasma. Due to their, compared to the other plasma components, macroscopic size, these grains become highly negatively charged on the one hand, but with their high mass move relatively slow on the millisecond time scale due to the low charge-to-mass ratio of the dust particles on the other hand.

Confined in an isotropic 3D trap, an ensemble of a finite number of dust particles arranges into an ordered structure under their mutual shielded Coulomb (Yukawa) interaction. The particles settle on spherical nested shells. Such a charged particle cluster is termed Yukawa ball [4]. The structural as well as the dynamical properties (normal modes, interactions forces, etc.) of these Yukawa balls have been studied intensively [5–9]. Also, the occurrence of metastable states as well as spontaneous configurational changes have been reported recently [10,11].

The nature of phase transitions in confined 2D systems has been studied by simulations and experiments as well, which concordantly report melting as a two-step process, where initially the orientational order vanishes and subsequently radial correlations are destroyed [12–14].

In infinite 3D Coulomb systems (screening parameter $\kappa = 0$), the solid-liquid transition occurs when the ratio of Coulomb to thermal energy Γ, defined as

$$\Gamma = \frac{Q^2}{4\pi\varepsilon_0 b_{\mathrm{ws}}} \frac{1}{k_{\mathrm{B}} T}, \tag{1}$$

where Q is the charge of the dust particles, $b_{\mathrm{ws}} = (3/4\pi n)^{1/3}$ is the Wigner-Seitz distance for density n, and T is the particles' kinetic temperature, exceeds a critical value of $\Gamma_{\mathrm{crit}} \approx 170$, see Ref. [15]. For finite systems, Schiffer [16] has shown by means of simulations for harmonically trapped ions, that Γ_{crit} increases as the particle number decreases. With screening included, the critical coupling parameter increases roughly exponentially with the screening strength $\kappa = b_{\mathrm{ws}}/\lambda_{\mathrm{D}}$ [17], where λ_{D} is the (appropriate) shielding length.

Phase transitions in finite 3D systems are still an open issue for experiments. Here we will report on two different methods to drive the melting transition in finite 3D clusters (Yukawa balls). First, the transition is driven by changing the plasma conditions by increasing the plasma power. Second, heating by laser manipulation of the dust particles under constant plasma conditions is described.

The use of stereoscopic methods allows us to retrieve the full 3D particle dynamics in the cluster during the melting process. Hence, correlation functions can be measured in full quantitative detail. From the experiment, the critical Coulomb coupling parameter for the melting is determined and compared with first principle Monte Carlo simulations.

II. EXPERIMENT

The experiments have been performed in an asymmetric capacitively coupled rf discharge at 13.56 MHz. Generally, the setup is very similar to that reported in Refs. [7,11] (see Fig. 1). Argon was chosen as a working gas. The gas pressure was rather low between 6 and 8 Pa. The rf power was varied between 1.9 and 3.9 W (leading to $U_{\mathrm{pp}} \approx 65$–$85$ V) for the plasma-induced melting experiment. For the laser-induced melting transition, it was kept constant at 1.6 W ($U_{\mathrm{pp}} \approx 60$ V).

MF particles of 4.86 μm diameter were introduced by a dust dispenser. The particles are trapped inside a cubic glass box of

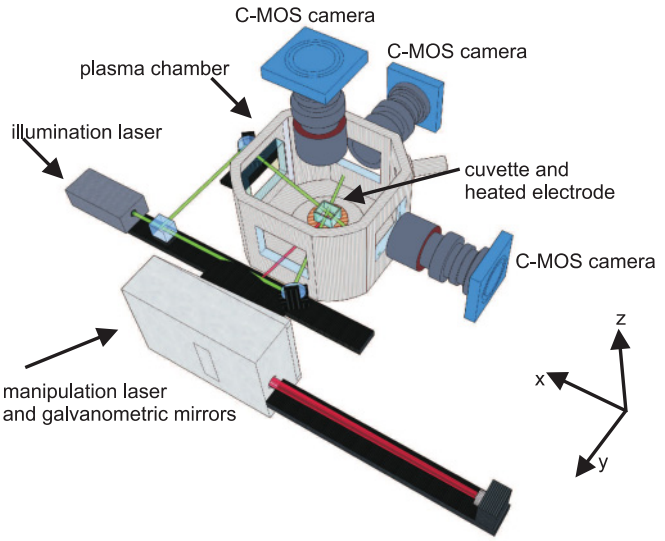

FIG. 1. (Color online) Scheme of the experimental setup used for the melting experiments. The particles confined in the glass box are illuminated by a Nd:YAG laser from two sides and manipulated by a diode laser from one side. The full 3D dynamics of all particles is measured with three orthogonal high-speed cameras.

2.5 cm wall length placed on top of the lower electrode. The forces that contribute to this confinement are gravity pointing downward, the electric field from the dielectric walls pointing inward, and a thermophoretic force due to a heated lower electrode assisted by the sheath electric field force levitate the particles against gravity [18]. The temperature of the heated electrode was adjusted to 65 °C.

For that condition, a few to about 80 particles are confined and form Yukawa balls for the melting experiments (see Fig. 2).

To measure the 3D particle positions, a stereoscopic imaging system was used consisting of three orthogonal CMOS cameras, which allow high speed imaging up to 500 fps and a maximum spatial resolution of 1280 × 1024 pixels. An expanded beam of a Nd:YAG laser of 600 mW maximum power was used to illuminate the particles from two sides. The trajectories presented here were recorded with a frame rate of 200 fps for the melting experiments. The 3D reconstruction was described in Refs. [11,19]. This allows us to measure the

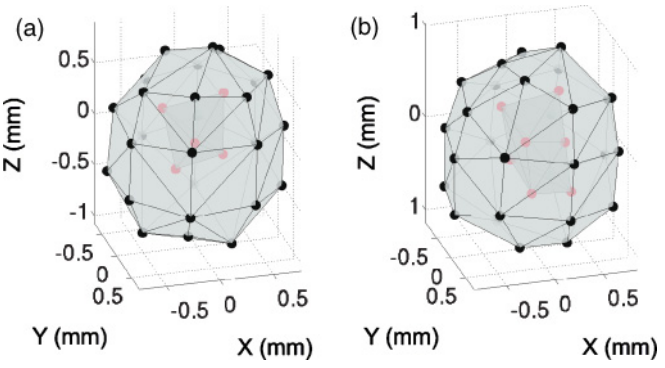

FIG. 2. (Color online) Structure of the investigated Yukawa balls. (a) $N = 32$ for the plasma-induced melting experiment and (b) $N = 35$ for the laser-induced melting experiment. The structure of the balls is influenced by the ion focus (see text).

full 3D dynamics of all individual particles in the cluster for more than 2000 frames.

For the plasma-induced melting experiments, the rf plasma power was changed, thereby exciting the Schweigert instability [20]. For the laser-induced melting, the particles were manipulated using a diode laser at 660 nm wavelength with a maximum power of 1 W. Via two galvanometric mirrors, the laser beam pointing along the y axis was swept randomly over the dust cloud, an approach which was used in a similar manner for finite 2D systems previously [21]. At each random position, the beam stayed fixed for $\tau = 0.1$ s, which determines the time scale of the laser-particle interaction, and then the beam was rapidly pointed to the next random position. Alternative approaches in other experiments [22] used Lissajous figures to laser heat extended crystal patches.

III. MELTING QUANTITIES

The identification of an exact melting point is difficult for finite systems. Due to the low number of particles in the system, thermodynamic quantities do not show a sharp transition point [13,16]. Moreover, in finite 2D systems, simulations have shown that the phase transition occurs in two steps, starting with a loss of orientational correlation, followed by a loss of radial correlation [12]. Similar behavior was found for the melting of finite 3D clusters with pure Coulomb interaction [23,24]. In the solid phase of a finite cluster one would expect orientational and radial order, whereas in the liquid, melted state orientational and radial order is lost.

For an infinite 3D system with Yukawa interaction, a distance fluctuation of about 16% to 19% would indicate melting [25], but this so-called Lindemann criterion has been found to be not directly applicable for systems with a finite particle number. In finite systems, usually the relative interparticle distance fluctuation (IDF)

$$u_{\mathrm{rel}} = \frac{2}{N(N-1)} \sum_{1 \leqslant i < j}^{N} \sqrt{\frac{\langle r_{ij}^2 \rangle}{\langle r_{ij} \rangle^2} - 1} \tag{2}$$

is determined. Here $r_{ij} = |\mathbf{r}_i - \mathbf{r}_j|$ is the distance between particles i and j, N is the total particle number, and $\mathbf{r}_i$ is the particle position relative to the center of the trap, respectively. To classify local disorder, we utilize the fluctuations of individual particles within the cluster according to

$$u_i = \frac{1}{N-1} \sum_{j \neq i} \sqrt{\frac{\langle r_{ij}^2 \rangle}{\langle r_{ij} \rangle^2} - 1}. \tag{3}$$

The IDF then follows by averaging over the individual fluctuations $u_{\mathrm{rel}} = N^{-1} \sum_{i=1}^{N} u_i$.

Böning *et al.* [26] proposed to use the variance of interparticle distance fluctuation (VIDF) to quantify the melting transition in finite systems. The VIDF can be used as an indicator of melting since it is found to be small for the solid and fluid phase, but large during the melting transition [26]. However, practically a reliable determination of the variance is not possible in the experiments since it would require an unachievably long time series. Hence we restrict to the IDF and the individual fluctuations u_i.

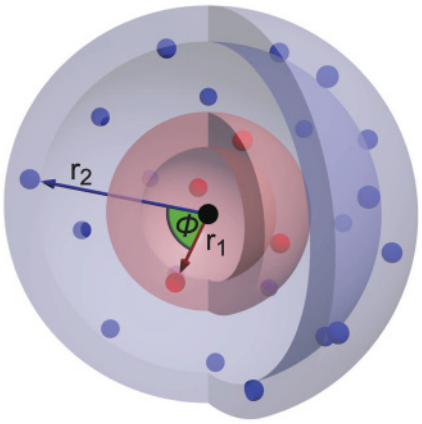

FIG. 3. (Color online) Scheme of the centered triple correlation function $g(r_1,r_2,\phi)$: r_1 (r_2) denotes the distance from the trap center to the first (second) particle and ϕ is the angle between the two vectors with respect to the trap center.

Another experimentally accessible quantity is the kinetic temperature of the particles. From the frame rate and the reconstructed particle positions, the velocity of each particle is easily calculated. The dust kinetic temperature is then found as

$$\frac{m}{2}\langle v_\alpha^2\rangle = \frac{k_B}{2}T_\alpha, \quad \alpha = x, y, z. \tag{4}$$

While this definition is strictly adequate only for systems with a Maxwellian velocity distribution, here it is used to characterize the kinetic energy of the cluster particles in the different spatial directions.

Finally, to get insight into the internal structure of these finite 3D systems, we use the so-called triple correlation function (TCF) $g(r_1,r_2,\phi)$ [27]. The TCF indicates the probability of finding a particle at a distance r_2 relative to the center of the confinement when a reference particle is located under an angle ϕ at a radial position r_1 (see Fig. 3). For the plots shown here, only particles on the inner shell were selected as a reference. Consequently g is integrated over the inner shell (r_1), resulting in $\bar{g}(r_2,\phi)$, where for convenience the maximum of $\bar{g}(r_2,\phi)$ is normalized to unity. Compared to the usual pair distribution function, the main advantage of the TCF is that it provides information about radial and orientational correlations simultaneously.

Two different scenarios of melting of finite 3D clusters are compared. First, the finite system is melted using a change of rf plasma power thus changing the plasma properties. Second, the method of laser heating is applied to achieve a phase transition. The latter one is an ideal tool to feed the systems kinetic energy without changing the plasma environment.

IV. PHASE TRANSITION BY CHANGING THE PLASMA ENVIRONMENT

We start with the analysis of the phase transition of Yukawa balls by increasing the rf power fed to the plasma.

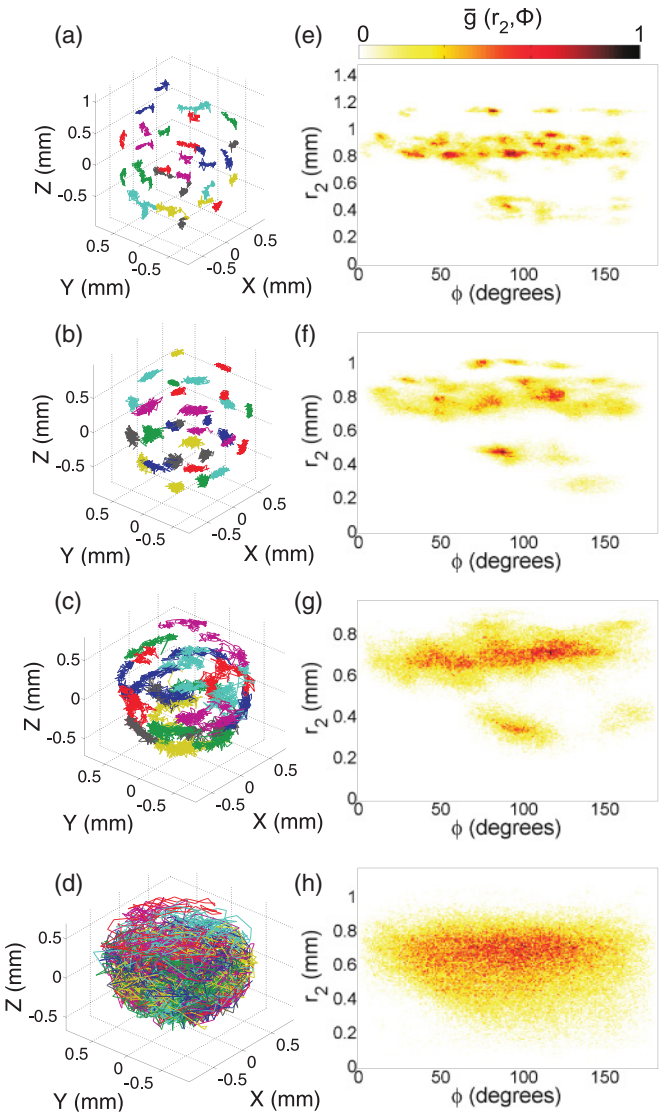

FIG. 4. (Color online) Trajectories of the Yukawa ball with $N = 32$ particles for (a) 1.9 W, (b) 2.3 W, (c) 2.7 W, and (d) 3.9 W. (e)–(h) $\bar{g}(r_2,\phi)$ for the corresponding clusters in (a)–(d).

A. Orientational and radial melting

As a representative, a cluster with $N = 32$ particles is investigated [see Fig. 2(a)]. The Yukawa ball consists of two shells, with 5 particles in the inner shell and 27 particles on the outer shell. Figures 4(a)–4(d) shows the Yukawa ball for an rf power that was increased from 1.9 to 3.9 W. For better visibility of the trajectories, a constant, very slow rotation of the entire cluster about the z axis is removed. For the lowest plasma power (i.e., 1.9 W) the particles within the cluster perform small excursions about their equilibrium positions only. The cluster is seen to be in a solid-like state [Fig. 4(a)].

Changing the plasma power leads to an increase of the energy of the Yukawa ball, as can be seen from the trajectories of the cluster [Figs. 4(b)–4(d)]. With increasing plasma power, the amplitude of the particles' excursions about their equilibrium positions start to grow. While for lower rf powers the particles still can be attributed to distinct shells, particle

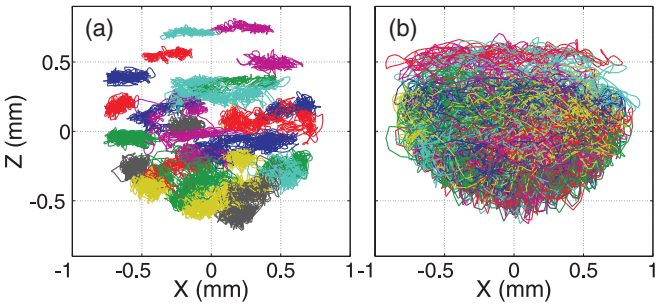

FIG. 5. (Color online) Side view of the cluster trajectories for $N = 32$ for an rf power of (a) 2.7 W and (b) 3.9 W.

exchanges start to occur at rf powers of about 2.7 W [see Fig. 4(c)]. Particles traveling between shells can indicate the onset of phase changes [6]. Note that in the upper part of the cluster, the particles move preferably in the horizontal xy plane, whereas the lower particles show large vertical displacements. This is illustrated also in a side view in Fig. 5(a). For the highest plasma power in this experiment, 3.9 W, no pronounced structure of the Yukawa ball remains [see Figs. 4(d) and 5(b)].

To quantify this phase transition, first of all, we look at the correlations within the cluster by means of the TCF. The TCF is shown in Figs. 4(e)–4(h), whereas darker colors indicate a higher correlation (the color plots are normalized to their respective maximum).

For the lowest input power considered, 1.9 W, one finds several peaks in the TCF for two pronounced radii around 0.4 and around 1.0 mm [see Fig. 4(e)]. These are, of course, the radii of the inner and outer shell, respectively. The outer shell has a pronounced substructure with three radial positions in the range between 0.8 and 1.1 mm. Furthermore, the TCF is peaked at distinct angular positions. These peaks indicate fixed orientational relations between the particles of the different shells. They are a direct indicator for radial and orientational order reflecting the solid-like state of the observed cluster. At input power of 2.3 W [Fig. 4(f)] one finds changes in the structure of the TCF. In particular, the number of angular peaks is reduced, and also the subshell structure around $r \approx 1$ mm appears diminished. At a plasma power of 2.7 W, the orientational order vanishes completely in Fig. 4(g), and the substructure of the outer shell is destroyed. For the power of 3.9 W, radial and orientational order are completely gone. The TCF shows only one continuous domain for various angles and radii [Fig. 4(h)].

Whereas the TCF resolves the orientational and radial order simultaneously, summing over the radial coordinate of the TCF $g(\phi) = \sum_{r_2} \bar{g}(r_2,\phi)$ will gain insight into the orientational order and, vice versa, summation over angle $g(r) = \sum_{\phi} \bar{g}(r_2,\phi)$ describes radial order. This is shown in Fig. 6. Since the work of Bedanov *et al.* [12], trapped finite clusters with Coulomb interaction are known to melt in two steps: first, by a loss of orientational correlation, followed by a loss of radial correlation at further increased heating. Such a behavior was already experimentally reported for finite 2D systems [14]. For the situation of 3D clusters considered here, a similar behavior is seen. The orientational order in Fig. 6(a) is clearly visible for 1.9 W indicated by the numerous distinct

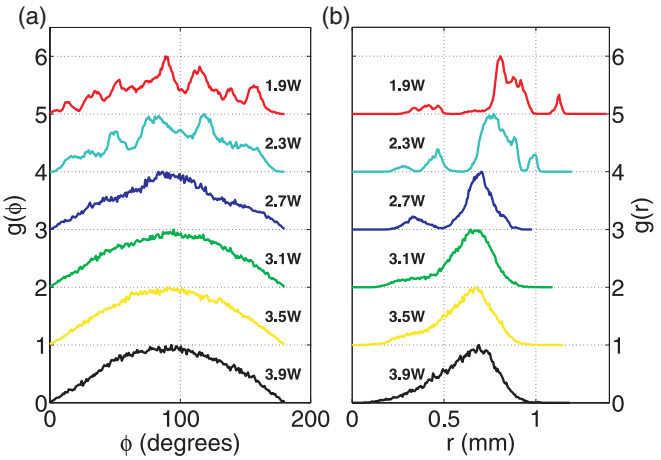

FIG. 6. (Color online) (a) Angular correlation $g(\phi)$ and (b) radial correlation $g(r)$ for a change of plasma power. For better visibility, the maximum of the correlation functions is normalized to unity and the curves are plotted with a constant offset of 1.

peaks. The orientational peaked structure decreases during the change of plasma power from 1.9 to 2.3 W, and finally disappears at 2.7 W.

The situation is different for the radial order [see Fig. 6(b)]. Here, at low plasma powers, distinct radial peaks (shells with substructure) are seen. The two peaks for the radial shell positions remain even for 2.7 W, where two shells are clearly seen (although the substructure has vanished). When one increases the driving plasma power to even higher values, as shown here for 3.9 W, the radial order also vanishes, as indicated by the broad structureless peak.

Another interesting feature concerns the confinement. As reported above, the confinement is only possible due to the equilibrium of several forces. An increased plasma density will also lead to stronger gradients in the sheath electric fields. Additionally, a higher plasma density leads to stronger screening. Both effects contribute to the shrinking of the observed cluster from 1.1 to about 0.7 mm in diameter during the change of the applied plasma power, which is easily seen in the radial shift of the peaks in Fig. 6(b).

To summarize this part, the TCF is an ideal tool to characterize the melting process. During increase of rf power the structure of the Yukawa ball first shows a loss of orientational order followed in a second step by the decay of radial order.

B. Melting parameters

Figure 7(a) shows the kinetic temperatures of the particles in all three spatial directions as a function of the applied plasma power determined according to Eq. (4) from the particles' velocities. A monotonic increase of the temperatures is clearly observable with rf plasma power. It is noticeable that the kinetic energy is nearly equally distributed between the three coordinates for input powers up to 2.7 W. For plasma powers about 3.1 W, the temperatures in z direction is higher than in the horizontal xy plane. This might be attributed to a change of the external confinement from nearly isotropic to more flattened, oblate Yukawa balls. Under these conditions, more severe vertical excursions are observed [see also Fig. 5(b)].

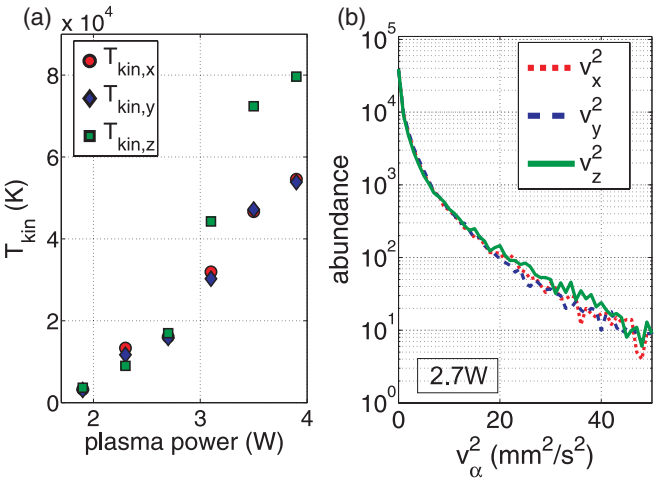

FIG. 7. (Color online) (a) Kinetic dust temperature as a function of applied plasma power for the three spatial directions. (b) Velocity distribution of all spatial directions for 2.7 W.

Note that the kinetic energies are relatively high even for low plasma power. For instance, a plasma power of 1.9 W leads to a mean kinetic energy of the particles of about 3100 K, which is roughly one order of magnitude higher than room temperature. This will be further discussed below.

Figure 7(b) shows the velocity distribution of the particles for a plasma power of 2.7 W. The distribution is nearly identical for all directions. The velocity distributions do not follow a single linear slope in this semilogarithmic representation and can therefore not be identified as a Maxwellian distribution function. Higher contributions are found for very small velocities. Nosenko *et al.* [22] attributed such a behavior to pixel locking artifacts in 2D images. In our case it might also be due to the limited spatial resolution of the 3D reconstruction.

The IDF was calculated for plasma-induced melting experiments as shown in Fig. 8 as a function of the applied plasma power. The IDF u_{rel} is small ($<10\%$) for plasma powers below 2.7 W and then increases to large values of $\approx 30\%$. The rise of the curve between 2.7 and 3.5 W ideally correlates with the transition from solid to liquid as derived from the TCF and indicates radial melting. Hence, the IDF as a global

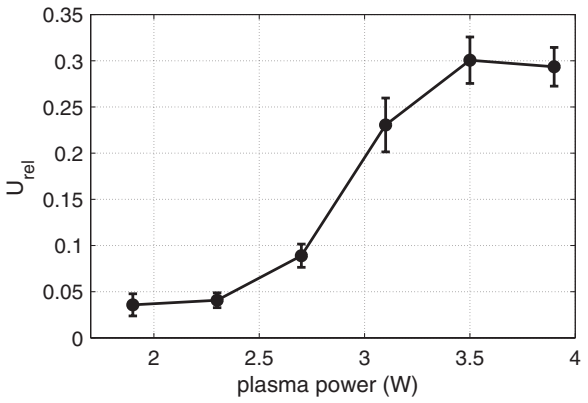

FIG. 8. Interparticle distance fluctuation (IDF) as function of applied plasma power. The error bars indicate the standard deviation of the individual IDF.

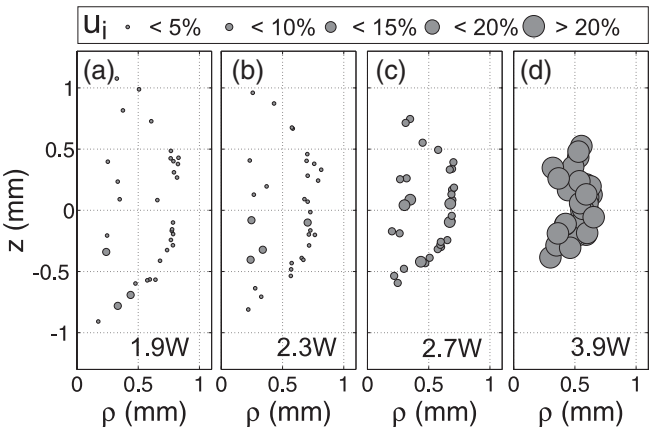

FIG. 9. Interparticle distance fluctuations for each particle in the ρ-z plot. The size of the markers corresponds to the magnitude of the fluctuations u_i. (a)–(d) Variation of plasma power.

parameter for the system supports the findings from the TCF. Interestingly, the Lindemann parameter for infinite 3D systems of about 16% to 19% at melting [25] matches the transition in this finite system.

To further understand the driving mechanism of the melting transition, we have investigated the fluctuations of every single particle within the cluster. This can be done by means of the individual distance fluctuation u_i according to Eq. (3). Figures 9(a)–9(d) shows the mean particle positions in cylindrical coordinates (ρ, z), with $\rho = \sqrt{(x^2 + y^2)}$ being the horizontal radius. Here the marker size is chosen according to the individual IDF of each particle, which means that a large circle indicates a large magnitude of the individual distance fluctuations.

For a plasma power of 1.9 W, one can see that the marker size and thus the fluctuations generally are small. The largest fluctuations are found in the lower part of the cluster. The situation is analogous for a plasma power of 2.3 W, but with overall larger fluctuations. In contrast, for a plasma power of 2.7 W, in the transition to the liquid state, all particles now show nearly the same fluctuation amplitudes. For a plasma power of 3.9 W [see Fig. 9(d)] large fluctuation magnitudes are seen, the cluster is in a fluid state.

Here and from Fig. 2 it can be seen that the particles are aligned vertically, the whole cluster is slightly elongated into the z direction instead of perfect spherical shape. Instead of onion-like shells, the arrangement of the cluster is influenced by the ion focus, which would be expected at these low gas pressures [28,29]. However, the chain-like structure is not as pronounced as in the experiments performed by Kroll *et al.* [28], but a vertical alignment of the particles is visible.

C. Discussion of plasma-driven melting

The higher fluctuations in the lower part of the cluster, the high kinetic temperatures well above room temperature even for low plasma powers, and the aligned structure of the observed clusters indicate that the driving mechanism for the plasma-induced phase transition is connected to the presence of the ion focus.

Ions streaming downward to the sheath of the discharge are focused below each negative dust particle and form a positive ionic space-charge region below the dust particles [20,30,31]. The ion focus is the reason for the structural properties of the observed dust systems, leading to chain-like structures [32–36]. Similarly for 3D clusters, an ion-wakefield attraction below each particle has been reported [28]. The presence of an ion focus leads to instabilities and energy transfer from the streaming ions to the dust [20,37]. Because of the nonreciprocal character of the wakefield attraction, the vertical alignment of the dust particles supports instabilities, since there are repulsive forces between the highly charged dust particles and attractive forces from the ion focus.

This is the reason for the heating of the particles within the cluster. This energy gain leads to melting of the cluster. The high kinetic energies of the dust particles within the cluster, even for a low plasma power of 1.9 W, are a direct hint for the role of the ion focus as an energy source. The increase of plasma power increases the action of the ion focus and the connected instabilities thus heating the cluster from the solid-like to the liquid-like state. As seen here, the instabilities start from the lower edge of the dust cloud [20]. These ion-focus induced instabilities have been found to be responsible for the melting transition of the multilayer 2D dust crystal embedded in the sheath of a discharge as well [20,37–39].

Another method to drive a transition to a liquid regime is the reduction of gas pressure. This pressure-induced transition was already studied intensively for 2D systems [38,39]. There a reduced pressure leads to a reduction of damping, which favors the instability. In larger 3D clouds a reduced gas pressure has been found to drive nonlinear dust acoustic waves [40–43].

We were also able to induce a phase transition by reducing the neutral gas pressure. However, with decreasing pressure the rf power also had to be increased to keep the cluster trapped. Hence the effect of decreasing pressure could not be studied without the effect of increased power and hence the effects of pressure reduction could not be separated from the effects of power increase and will not be further discussed.

V. PHASE TRANSITION VIA LASER HEATING

It is the great advantage of driving phase transitions by means of lasers that the plasma environment is unaffected by the laser, because the particles are pushed directly by the laser beam.

A. Orientational and radial melting

To investigate the laser-driven phase transition, a cluster consisting of $N = 35$ particles was randomly hit by a laser beam with laser powers up to 160 mW. In Figs. 10(a)–10(d) the trajectories of the cluster are shown for different laser heating powers. As above, a constant rotational motion of the whole clusters is subtracted. In the purely Brownian case with no applied laser power [Fig. 10(a)], basically the particles move around their equilibrium positions. However, an interesting phenomenon occurs. Several particles in the lower part of the cluster move over larger distances, which can be clearly seen

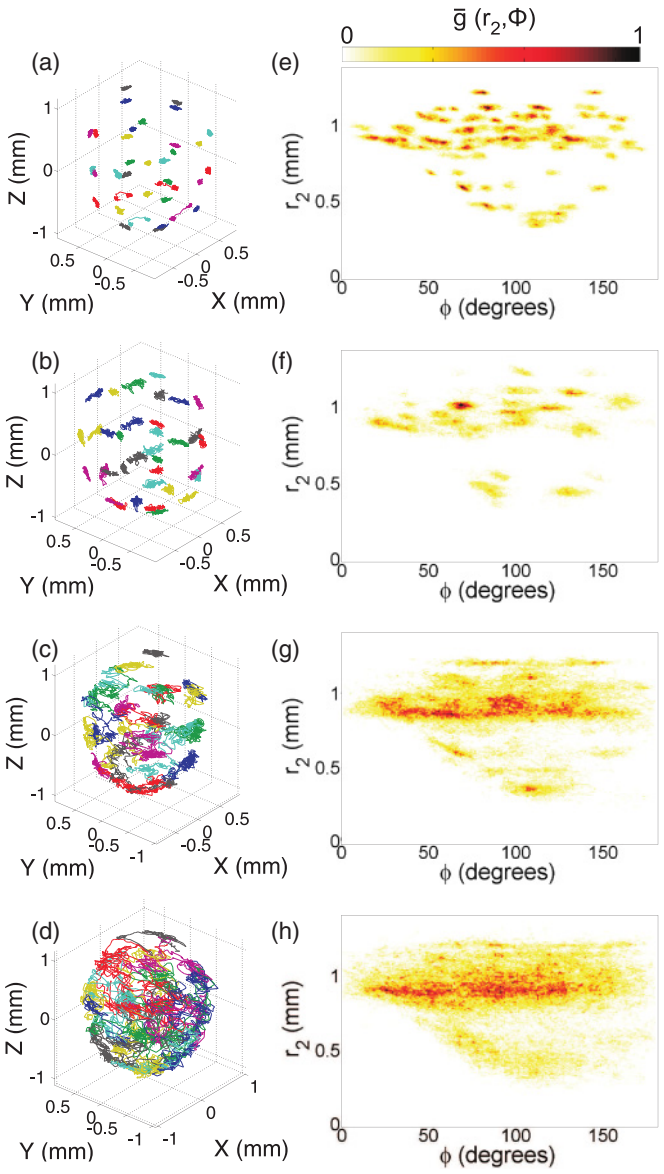

FIG. 10. (Color online) Trajectories for the Yukawa ball with $N = 35$ particles for laser heating with (a) 0 mW, (b) 50 mW, (c) 100 mW, and (d) 160 mW. (e)–(h) $\bar{g}(r_2,\phi)$ for the corresponding clusters in (a)–(d).

in the trajectories. Those spontaneous configuration changes are well known features for Yukawa clusters [11]. They emerge because different metastable states are energetically accessible, even at room temperature [10,11,44], since the energy differences between the ground state and metastable states are very small.

By heating the ensemble with low laser power of about 50 mW [Fig. 10(b)] only small displacements of the particles are visible. The situation changes, when the particles are "kicked" by medium laser powers of about 100 mW [see Fig. 10(c)]. Here the power is high enough to overcome the energy barriers for particle exchanges, all particles within the cluster show larger excursions, but the general structure of the ball remains. For the highest laser power used in this experiment, 160 mW [Fig. 10(d)], the ordered structure is destroyed.

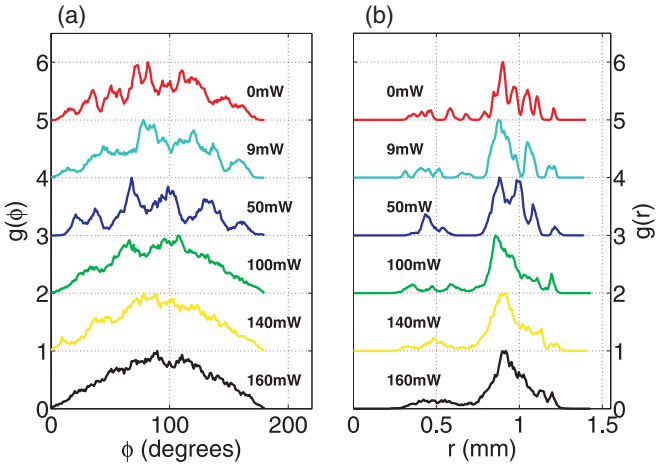

FIG. 11. (Color online) (a) Angular correlation $g(\phi)$ and (b) radial correlation $g(r)$ for a change of laser power. For better visibility the maximum of the correlation functions is normalized to unity and the curves are plotted with a constant offset of 1.

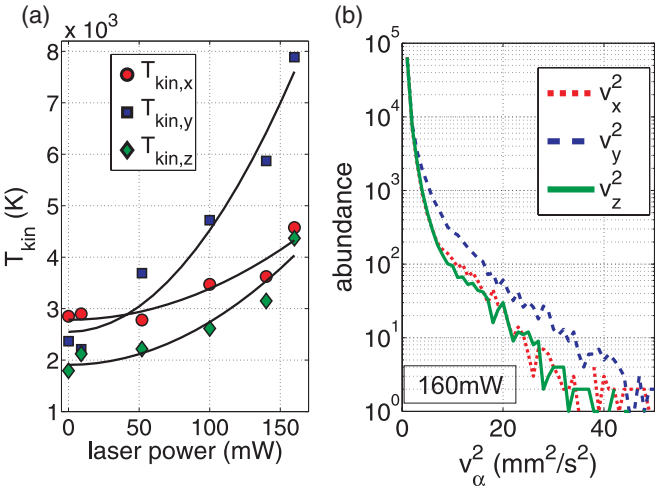

FIG. 12. (Color online) (a) Kinetic dust temperature as function of applied laser power. The solid lines represent parabolic fits to the experimental data. (b) Velocity distribution for a laser power of 160 mW.

To study the radial and orientational order during the laser induced melting transition, we again investigate the TCF for various different laser powers [see Figs. 10(e)–10(h)]. The TCF changes in a similar manner as in the plasma-induced melting experiment. With no externally applied laser heating [Fig. 10(e)], one finds a rich, peaked structure again, a sign for finite solid systems. For low input power from the laser of 50 mW [Fig. 10(f)], the peaked structure starts to diminish already. No pronounced angular peaks remain for input powers of about 100 mW, a broad continuous structure can be found in Fig. 10(g). For the highest laser power of 160 mW, finally also a loss of the radial structure is found [Fig. 10(h)].

To gain more insight into the orientational and radial order during this laser heating process, again the TCF was summed over the angles and radii (as shown in Fig. 11). For laser powers up to 50 mW, one finds a number of peaks for various angles and radii, indicating a highly ordered orientational and radial structure of the system. For laser power of 100 mW, the orientational order has nearly vanished, whereas the radial order is still intact. Even for the highest laser power, there are still two pronounced radial positions at about 0.5 and 0.9 mm. However, the radial order does not fall back to zero between the shells, indicating the presence of radial laser driven intershell particle exchanges.

Again, the orientational correlation is lost at ≈100 mW before the radial correlation at ≈140 mW, supporting that the phase transition occurs in two steps [12].

In contrast to the plasma-induced melting experiment, the cluster size stays the same for all applied laser powers. The peaks in $g(r)$ do not shift radially with applied laser power. This underlines that the method of laser heating behaves as a powerful tool to dissipate kinetic energy in the dusty plasma subsystem without changing the plasma environment itself.

B. Melting parameters

This leads us to the question, how particles interact with the laser. Since the laser beam is swept randomly from one side over the cross section of the cluster, particles within the cluster experience random kicks. Wolter *et al.* [21] used this method to drive phase transitions in 2D clusters. The laser-particle interaction is due to radiation pressure [45], leading to a quadratic dependence of the kinetic dust temperature from the applied laser power P_l [21]. This dependence, $T_{\rm kin} = T_0 + C \cdot P_l^2$, with T_0 being the kinetic temperature of the unheated particles, is also tested here for the three-dimensional case [see Fig. 12(a)], where the kinetic temperatures for all space directions are shown as a function of the applied laser power. As seen from Fig. 12(a), the temperature indeed scales with the applied laser power squared, supporting the assumption of radiation pressure.

Again, the kinetic energy $T_{\rm kin} \approx$ 2000–3000 K is much higher than room temperature even for no externally applied heating. As argued before, the reason is the energy gain due to the ion focus, which serves as a free source of energy. The energy is however not large enough to melt the cluster.

In contrast to the plasma-induced melting experiment, no equipartition of the kinetic energies in the different spatial directions is found. Here the laser beam, pointing in negative y direction, transfers more energy along the beam axis than perpendicular. Hence, the kinetic energy in the y component is higher than in x and z, which are roughly equal. The energy transfer to the other directions is assumed to be due to Coulomb collisions between the dust particles. This was also seen in the laser experiments on flat dust clouds [21,22]. The particle velocity distribution for a laser power of 160 mW [see Fig. 12(b)] supports this finding. The velocity is generally higher along the direction of the laser beam (y) as compared to the perpendicular coordinates (x,z). Again, the distribution function is not Maxwellian.

As in Sec. IV, the IDF is shown in Fig. 13 as a function of the applied laser power. Here an increase of the IDF $u_{\rm rel}$ can be found already for low laser powers of about 50 mW. For the maximum applied laser power the IDF is about $u_{\rm rel} = 18\%$. From the TCF this was identified as a melted state. Hence

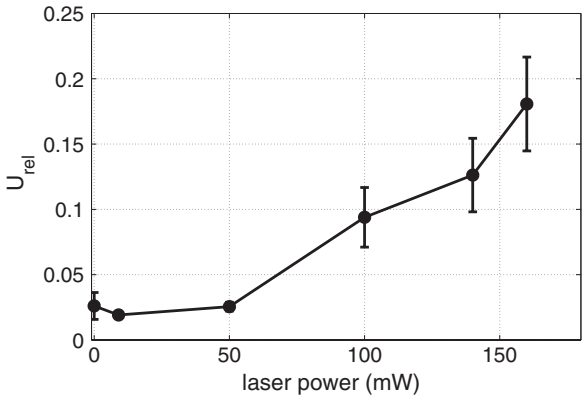

FIG. 13. Interparticle distance fluctuation (IDF) as function of applied laser power. The error bars indicate the standard deviation of the individual IDF.

again, the Lindemann criterion for infinite systems (melting between 16% and 19% fluctuation level) still is a good estimate for the phase transition for finite systems.

The individual particles fluctuations are shown in Figs. 14(a)–14(d). As done above, the mean particle positions are plotted in the ρ-z plane, and the size of the markers indicates the magnitude of the fluctuations. Like in the plasma-induced melting experiment, the structural properties of the presented clusters are influenced by the presence of positive ionic space charges, leading to an alignment of the particles in the clusters [cf. Figs. 2(b) and 14(a)–14(d)].

From laser power of 0 to 50 mW [Figs. 14(a) and 14(b)], the fluctuation magnitudes within the cluster look very similar. For laser powers of 100 mW [Fig. 14(c)], the distance fluctuations occur almost everywhere in the cluster. In the case of 160 mW [see Fig. 14(d)] the shell structure starts to diminish, the amplitudes of the fluctuations are reaching high values, and the cluster is in a fluid-like state.

In contrast to the plasma-melting experiment, no melting from "bottom up" occurs, rather the cluster is heated throughout. This also underlines the different driving mechanism of the transition.

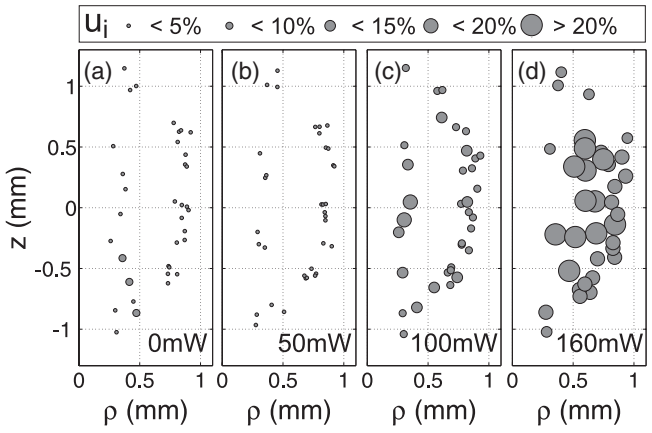

FIG. 14. Interparticle distance fluctuations for each particle in the ρ-z plot. The size of the markers corresponds to the magnitude of the fluctuations u_i. (a)–(d) Variation of laser power.

C. Determination of coupling strength

To compare the expectations for melting in Yukawa systems, the value of Γ was calculated according to Eq. (1) from the laser heating experiment. Therefore, the melting point is decided to be at a laser power of 140 mW because at this laser power the orientational order is already lost and the radial order starts to diminish as shown above. For a laser power of 140 mW, the kinetic temperatures of the particles are strongly anisotropic in the different spatial directions and were determined as $T_{\mathrm{kin}} = (4200 \pm 1500)$ K.

The most crucial parameter for the estimation of a critical Γ is the dust charge. Several parameters of the discharge are required for a quantitative determination of the charge. We have applied the collision-reduced charging model of Khrapak *et al.* [46]. For this experiment, the mean free path length was computed using the collision cross section $\sigma = 85 \times 10^{-20}$ m^2 from Ref. [47]. Arp *et al.* [18] performed simulations for a discharge vessel similar to our experiment and derived a plasma density of $n_e \approx 5 \times 10^{13}$ m^{-3} and an electron temperature of $T_e \approx 3$ eV. Using the approach of Khrapak *et al.* [46], the charge of a dust particle is then determined as $Q \approx 6900 \pm 1000$ elementary charges, where the error in the dust charge mainly is due to the plasma density.

Usually, in finite systems, one would use the definition of $r_0 = (Q^2/2\pi m \varepsilon_0 \omega_0^2)^{1/3}$, with Q and m being charge and mass of the particle and ω_0 being the strength of the external confinement, as a measure for the typical interparticle spacing [13]. This would require the knowledge of the confinement frequency ω_0. Here, in contrast, the Wigner-Seitz radius b_{ws} in the definition given above is used for our analysis where the dust density is derived from the cluster size and the number of particles in the cluster. It is found as $b_{\mathrm{ws}} = 330$ μm. Using a dust charge of $Q = (6900 \pm 1000)e$, a Wigner-Seitz radius of $b_{\mathrm{ws}} = 330$ μm and the dust temperature of $T_{\mathrm{kin}} = (4200 \pm 1500)$ K, we obtain a critical coupling parameter of

$$\Gamma_{\mathrm{crit}} = 570 \pm 270 \tag{5}$$

for a cluster of $N = 35$ particles. Here the error in Γ_{crit} takes into account the uncertainties in the dust temperature as well as in the estimated dust charge.

This value seems to be too high for the melting of Yukawa systems at first glance, but has to be discussed in more detail. First, the measured velocity distribution shows strong deviations from a Maxwellian distribution, with a high contribution especially of slow velocities. Therefore, the estimated temperature has the trend to be too low for all spatial directions. With higher temperatures, one would expect a lower value of Γ_{crit}.

Also, additional factors have to be taken into account for finite Yukawa clusters, namely screening by the ambient plasma and the finite number of involved particles. The latter one was investigated by Schiffer [16], who gave an empirical relation for calculating a critical Γ for finite systems in the case of pure Coulomb interaction

$$\Gamma_{\mathrm{fin}} = \Gamma_0 \frac{1}{1 - 0.98 \cdot F}. \tag{6}$$

Here $\Gamma_0 \approx 170$ is the critical coupling parameter for infinite matter [15] and F is the fraction of particles in the outer shell.

If we adopt this formula for a Yukawa ball with 35 particles and 28 particles at the outer shell, F becomes 28/35. Hence the critical value of Γ_{fin} is obtained as

$$\Gamma_{\mathrm{fin}} \approx 790,$$

which is in the range of our deviations. Additionally, screening by the ambient plasma will also influence melting. Vaulina *et al.* [48] derived a scaling law of the form

$$\Gamma^* = \Gamma\left(1+\kappa+\frac{\kappa^2}{a}\right)^{-1}\exp(\kappa) \tag{7}$$

to describe melting under the influence of shielded interaction, where $a = 2$ for an infinite system. For a finite cluster a may depend on N, for $N = 2$ one finds $a = 3$ [5,49]. For usual Yukawa ball experiments, κ is in the range between 0.5 and 1.5, see Ref. [10]. In that region, Γ^* is only a weakly dependent on κ: $\Gamma^*/\Gamma = 1.01$–1.23 for $a = 2$ and $\Gamma^*/\Gamma = 1.04$–1.38 for $a = 3$, according to Eq. (7). Combining the influence of shielding and the finite system size one would expect the critical Γ to be in the range from $\Gamma = 800$–1000, which is even somewhat larger than our measurements.

VI. COMPARISON WITH MONTE CARLO RESULTS

At this point, the question arises, how the results above can be understood and reproduced within a simple isotropic Yukawa model. To that end we employ a spherical parabolic confinement potential in which the N identical dust grains are trapped

$$H_N = \sum_{i=1}^{N-1}\sum_{j>i}^{N}\frac{Q^2}{4\pi\varepsilon_0}\frac{e^{-\kappa|\mathbf{r}_i-\mathbf{r}_j|}}{|\mathbf{r}_i-\mathbf{r}_j|}+\sum_{i=1}^{N}\frac{m}{2}\omega_0^2 r^2. \tag{8}$$

The configurational space is sampled with respect to the Boltzmann factor e^{-H_N/k_BT}, using Eq. (8), by means of thermodynamic Monte Carlo simulations within the (N,V,T) ensemble (for details on the utilized standard Metropolis algorithm see Ref. [3]). In other words, it samples the probability distribution within the thermodynamic equilibrium for a given temperature and particle number. The grain charge Q, mass m, and trap frequency ω_0 define as above the base unit of length $r_0 = (Q^2/2\pi\varepsilon_0 m\omega_0^2)^{1/3}$. In these units we take $\kappa = 1.26$ in the simulations. The coupling parameter Γ was computed as in the experiment.

The Monte Carlo results for $N = 32$ are presented in Fig. 15 and should be compared to the experiment in Fig. 4. In the Yukawa crystal phase ($\Gamma = 16\,000$), a subshell structure is observed, see also Fig. 16. When Γ is decreased to 1600, these pronounced subshells vanish on both shells. The orientational order within the shell holds up to $\Gamma \approx 380$. Finally, the radial order, that is, the formation of shells, is lost for $\Gamma \lesssim 70$.

The general trend observed in the simulation coincides with the experiment. In Fig. 15(d), corresponding to a Γ of about 12, it is seen that the TCF shows only one continuous domain which looks very similar to the TCF for high plasma powers, see Fig. 4(h). For a higher Γ of roughly 150, the TCF's in Fig. 15(c) and for comparison Fig. 4(g) are both characterized by the emergence of the two shell structure, while the orientational correlation is still not built up. For higher values of the coupling parameter, that is, $\Gamma \geqslant 1600$ [see Figs. 15(a) and 15(b)], the TCFs can be attributed to Fig. 4(e) or 4(f), where the experimental cluster is in a solid-like state. Differences between experiment and simulation are mainly due to the fact that the simulations assume an isotropic Yukawa interaction, whereas the clusters observed in the experiment are influenced by the presence of the ion focus.

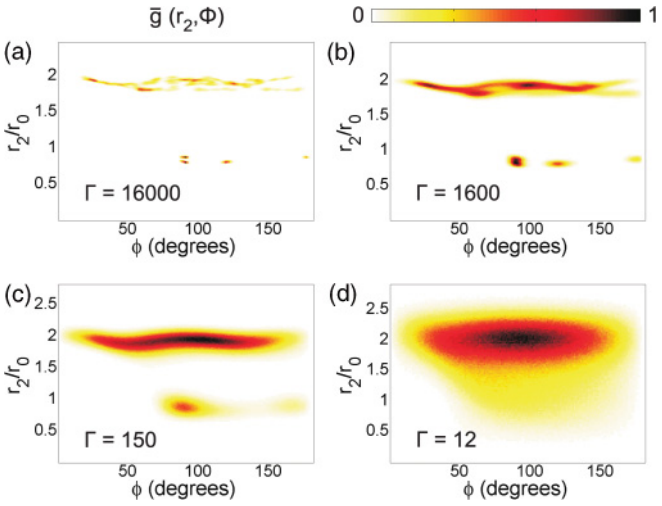

FIG. 15. (Color online) TCF obtained from Monte Carlo calculations for $N = 32$, $\kappa = 1.26$, and $\Gamma \approx 12$, 150, 1600, and 16 000. The grains form shells in the range $12 < \Gamma_{\mathrm{crit}}^{\mathrm{rad}} < 150$ and become localized within the shells (orientational ordered) for $150 < \Gamma_{\mathrm{crit}}^{\mathrm{ang}} < 1600$.

Similar to the experiment, radial and orientational correlations are investigated by means of the radially and angular integrated TCF (see Fig. 16). The radially integrated TCF [Fig. 16(a)] shows a structureless orientational distribution for $\Gamma = 45$ which corresponds to high plasma powers in the experiment. A single peak at 90° starts to form in the range $\Gamma = 150$–500, which in the same manner arises for medium plasma powers [see Fig. 6(a)]. Additional peaks appear for $\Gamma \gtrsim 1600$ which correspond to an orientational order as in the

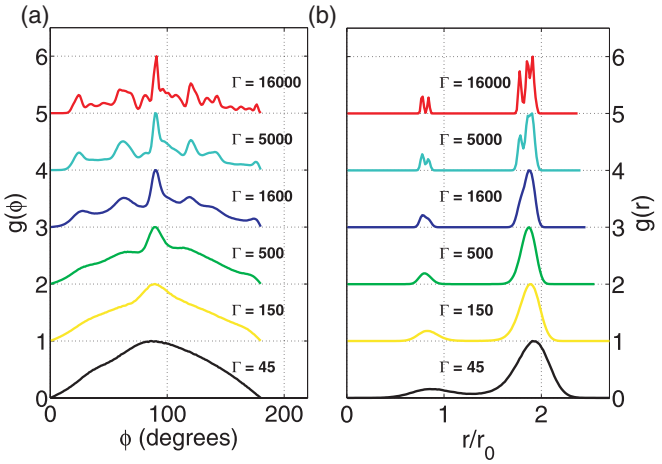

FIG. 16. (Color online) (a) Angular correlation $g(\phi)$ and (b) radial correlation $g(r)$ for a change of coupling strength in the Monte Carlo simulations for $N = 32$. For better visibility the maximum of the correlation functions is normalized to unity and the curves are plotted with a constant offset of 1.

experiment. The angular integrated TCF [Fig. 16(b)] shows for $\Gamma = 45$ an (slight) inner and an outer peak which indicate the emergence of the two shell structure. For $\Gamma = 150$–1600 there are two distinct peaks which are, however, wider separated than the two peaks seen in the experiment. In the simulation subshells emerge for $\Gamma > 1600$, while in the experiment fine structured radial order appears for low plasma power, see Fig. 6, respectively. In particular, the third outer main peak observed in the experiment does not appear in the simulations. These deviations must be attributed to additional plasma correlation effects which are not covered by the simple one-component dust model considered here. Such additional effects may involve modifications of the external confinement potential or an anisotropic grain interaction potential due to plasma streaming [50].

VII. SUMMARY

Two different melting scenarios for 3D finite dust clusters (Yukawa balls) in a plasma environment were presented. The TCF was systematically applied to investigate correlations in the cluster.

At first, the method of increasing the plasma power was used to yield a plasma-induced melting scenario. Here it was found that increasing the plasma power leads to increasing disorder in the cluster. The TCF loses the peaked structure, indicating the loss of the orientational and radial order.

The driving mechanism for the plasma-induced melting is the ion focus. Streaming ions focused below each dust particle are a source of free energy for the dust particles. These findings are supported by the high kinetic temperatures of the dust particles even at sufficiently low plasma powers. Additionally, the positive space charge modifies the structure of the observed Yukawa balls, leading to vertical alignment of particles. The melting starts at the bottom of the cluster.

Second, the method of laser heating was used to drive the phase transition of Yukawa balls. In contrast to the plasma-induced melting scenario, the plasma environment is unaffected by the laser beams. The dust particles are heated directly by the beam. An increased heating leads to a decrease of order, too. Unlike the plasma-induced melting, the heating by random kicks due to the laser is directly responsible for the phase transition due to the transfer of kinetic energy to the particles. In both considered melting scenarios, the orientational order is lost before the radial order vanishes. The critical coupling parameter for melting is found to be $\Gamma \approx 570$, which can be understood from the finite size and screening effects of the system.

ACKNOWLEDGMENTS

This work is supported by the Deutsche Forschungsgemeinschaft via SFB-TR24 Grants A2, A3, A5, and A7.

[1] P. K. Shukla and A. A. Mamun, *Introduction to Dusty Plasma Physics* (Institute of Physics Publishing, Bristol, 2002).
[2] G. E. Morfill and A. V. Ivlev, Rev. Mod. Phys. **81**, 1353 (2009).
[3] M. Bonitz, N. Horing, and P. Ludwig, Eds., *Introduction to Complex Plasmas*, Springer Series on Atomic, Optical, and Plasma Physics (Springer, New York, 2010).
[4] O. Arp, D. Block, A. Piel, and A. Melzer, Phys. Rev. Lett. **93**, 165004 (2004).
[5] M. Bonitz, D. Block, O. Arp, V. Golubnychiy, H. Baumgartner, P. Ludwig, A. Piel, and A. Filinov, Phys. Rev. Lett. **96**, 075001 (2006).
[6] D. Block, M. Kroll, O. Arp, A. Piel, S. Käding, Y. Ivanov, A. Melzer, C. Henning, H. Baumgartner, P. Ludwig, and M. Bonitz, Plasma Phys. Controlled Fusion **49**, B109 (2007).
[7] Y. Ivanov and A. Melzer, Phys. Rev. E **79**, 036402 (2009).
[8] T. Antonova, B. M. Annaratone, D. D. Goldbeck, V. Yaroshenko, H. M. Thomas, and G. E. Morfill, Phys. Rev. Lett. **96**, 115001 (2006).
[9] T. Antonova, B. M. Annaratone, H. M. Thomas, and G. E. Morfill, New J. Phys. **10**, 043028 (2008).
[10] D. Block, S. Käding, A. Melzer, A. Piel, H. Baumgartner, and M. Bonitz, Phys. Plasmas **15**, 040701 (2008).
[11] S. Käding, D. Block, A. Melzer, A. Piel, H. Kählert, P. Ludwig, and M. Bonitz, Phys. Plasmas **15**, 073710 (2008).
[12] V. M. Bedanov and F. M. Peeters, Phys. Rev. B **49**, 2667 (1994).
[13] V. A. Schweigert and F. M. Peeters, Phys. Rev. B **51**, 7700 (1995).
[14] Y. Ivanov and A. Melzer, Phys. Plasmas **12**, 072110 (2005).
[15] S. Ichimaru, Rev. Mod. Phys. **54**, 1017 (1982).
[16] J. P. Schiffer, Phys. Rev. Lett. **88**, 205003 (2002).
[17] S. Hamaguchi, R. T. Farouki, and D. H. E. Dubin, Phys. Rev. E **56**, 4671 (1997).
[18] O. Arp, D. Block, M. Klindworth, and A. Piel, Phys. Plasmas **12**, 122102 (2005).
[19] Y. Ivanov and A. Melzer, Rev. Sci. Instrum. **78**, 033506 (2007).
[20] V. A. Schweigert, I. V. Schweigert, A. Melzer, A. Homann, and A. Piel, Phys. Rev. E **54**, 4155 (1996).
[21] M. Wolter and A. Melzer, Phys. Rev. E **71**, 036414 (2005).
[22] V. Nosenko, J. Goree, and A. Piel, Phys. Plasmas **13**, 032106 (2006).
[23] S. W. S. Apolinario and F. M. Peeters, Phys. Rev. E **76**, 031107 (2007).
[24] S. W. S. Apolinario and F. M. Peeters, Phys. Rev. B **78**, 024202 (2008).
[25] E. J. Meijer and D. Frenkel, J. Chem. Phys. **94**, 2269 (1991).
[26] J. Böning, A. Filinov, P. Ludwig, H. Baumgartner, M. Bonitz, and Y. E. Lozovik, Phys. Rev. Lett. **100**, 113401 (2008).
[27] P. Ludwig, H. Thomsen, K. Balzer, A. Filinov, and M. Bonitz, Plasma Phys. Controlled Fusion **52**, 124013 (2010).
[28] M. Kroll, J. Schablinski, D. Block, and A. Piel, Phys. Plasmas **17**, 013702 (2010).
[29] C. Killer, A. Schella, T. Miksch, and A. Melzer, Phys. Rev. B **84**, 054104 (2011).
[30] M. Nambu, S. V. Vladimirov, and P. K. Shukla, Phys. Lett. A **203**, 40 (1995).

[31] M. Lampe, G. Joyce, and G. Ganguli, Phys. Plasmas **7**, 3851 (2000).
[32] J. H. Chu and L. I, Phys. Rev. Lett. **72**, 4009 (1994).
[33] K. Takahashi, T. Oishi, K. I. Shimomai, Y. Hayashi, and S. Nishino, Phys. Rev. E **58**, 7805 (1998).
[34] A. Melzer, V. A. Schweigert, and A. Piel, Phys. Rev. Lett. **83**, 3194 (1999).
[35] V. Steinberg, R. Sütterlin, A. V. Ivlev, and G. Morfill, Phys. Rev. Lett. **86**, 4540 (2001).
[36] A. Piel, Phys. Plasmas **18**, 073704 (2011).
[37] A. Melzer, V. A. Schweigert, I. V. Schweigert, A. Homann, S. Peters, and A. Piel, Phys. Rev. E **54**, 46 (1996).
[38] A. Melzer, A. Homann, and A. Piel, Phys. Rev. E **53**, 2757 (1996).
[39] H. Thomas and G. E. Morfill, Nature (London) **379**, 806 (1996).
[40] M. Schwabe, M. Rubin-Zuzic, S. Zhdanov, H. M. Thomas, and G. E. Morfill, Phys. Rev. Lett. **99**, 095002 (2007).
[41] R. L. Merlino, Phys. Plasmas **16**, 124501 (2009).
[42] T. M. Flanagan and J. Goree, Phys. Plasmas **17**, 123702 (2010).
[43] T. M. Flanagan and J. Goree, Phys. Plasmas **18**, 013705 (2011).
[44] A. Melzer, S. Käding, D. Block, and A. Piel, J. Phys. Condens. Matter **20**, 404204 (2008).
[45] B. Liu, J. Goree, V. Nosenko, and L. Boufendi, Phys. Plasmas **10**, 9 (2003).
[46] S. A. Khrapak *et al*., Phys. Rev. E **72**, 016406 (2005).
[47] M. A. Lieberman and A. J. Lichtenberg, *Principles of Plasma Discharges and Materials Processing* (John Wiley, New York, 1994).
[48] O. S. Vaulina and S. A. Khrapak, JETP **90**, 287 (2000).
[49] T. Ott, M. Stanley, and M. Bonitz, Phys. Plasmas **18**, 063701 (2011).
[50] M. Lampe, G. Joyce, and G. Ganguli, IEEE Trans. Plasma Sci. **33**, 57 (2005).